NANO LETTERS

Letter

pubs.acs.org/NanoLett

Electromechanical Coupling among Edge Dislocations, Domain Walls, and Nanodomains in $BiFeO_3$ Revealed by Unit-Cell-Wise Strain and Polarization Maps

A. Lubk,*[,†,#] M. D. Rossell,[‡] J. Seidel,[§] Y. H. Chu,[∥] R. Ramesh,[⊥] M. J. Hÿtch,[#] and E. Snoeck[#]

[†]Triebenberg Laboratory, Institute of Structure Physics, Technische Universität Dresden, 01062 Dresden, Germany

[‡]Electron Microscopy Center, Empa, Swiss Federal Laboratories for Materials Science and Technology, CH-8600 Dübendorf, Switzerland

[§]Materials Science Division, Lawrence Berkeley National Laboratory, Berkeley, California 94720, United States

[∥]Department of Materials Science and Engineering, National Chiao Tung University, Hsinchu 30010, Taiwan

[⊥]Department of Materials Science and Engineering, University of California, Berkeley, California, United States

[#]CEMES-CNRS, Université de Toulouse, 29 rue Jeanne Marvig, 31055 Toulouse, France

Supporting Information

ABSTRACT: The performance of ferroelectric devices, for example, the ferroelectric field effect transistor, is reduced by the presence of crystal defects such as edge dislocations. For example, it is well-known that edge dislocations play a crucial role in the formation of ferroelectric dead-layers at interfaces and hence finite size effects in ferroelectric thin films. The detailed lattice structure including the relevant electromechanical coupling mechanisms in close vicinity of the edge dislocations is, however, not well-understood, which hampers device optimization. Here, we investigate edge dislocations in ferroelectric $BiFeO_3$ by means of spherical aberration-corrected scanning transmission electron microscopy, a dedicated model-based structure analysis, and phase field simulations. Unit-cell-wise resolved strain and polarization profiles around edge dislocation reveal a wealth of material states including polymorph nanodomains and multiple domain walls characteristically pinned to the dislocation. We locally determine the piezoelectric tensor and identify piezoelectric coupling as the driving force for the observed phenomena, explaining, for example, the orientation of the domain wall with respect to the edge dislocation. Furthermore, an atomic model for the dislocation core is derived.

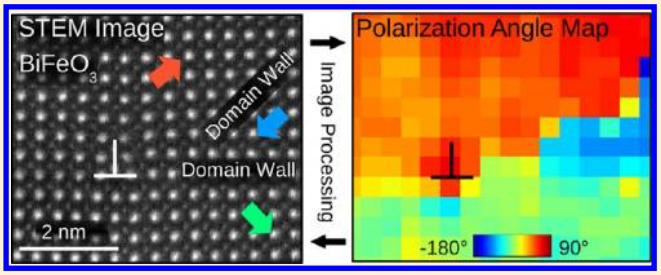

KEYWORDS: *Ferroelectricity, dislocation, domain wall, finite size effect*

Dislocation-type crystal defects are a typical feature of epitaxially grown thin films since they compensate misfit strains introduced by the lattice mismatch between film and substrate. In case of perovskite type ferroelectric thin films the formation of regular edge dislocation (ED) networks with mesh spacings determined by the lattice mismatch could be observed.[1,2] It was pointed out that these networks lead to a degradation of (ferro-)electric properties (phase transition temperature,[1,3,4] piezoelectric,[3] and dielectric response[5]) in a several nanometer thin layer at the interface. This so-called dead layer plays a crucial role in size effects[4] and limits the applicability of ferroelectric thin films in various applications, for example, actuators and capacitors. Furthermore, dislocations pin ferroelastic and ferroelectric domain walls (DW), thus reducing their mobility.[6−8] They can also play a crucial role in the exchange bias effect by providing locally uncompensated spins.[9] Generally, two separate regions divided by a certain transition zone can be distinguished when studying dislocations: (i) The core region as a material state of its own with different atomic coordination including broken or reconstructed bonds.[10] (ii) The surrounding region with a strained original bulk structure, defining the characteristic mechanical properties of the dislocation, e.g. the long-range strain field. Within the surrounding region, one can additionally distinguish the transition region close to the core, where strain can be very large affecting electronic and electric properties in a nonlinear fashion.[10] To obtain the spatially resolved lattice structure at EDs, aberration-corrected HR(S)TEM (high-resolution (scanning) transmission electron microscopy) studies are required, which are particularly demanding at perovskites due to the weakly scattering O atoms. Thus only a relatively small number of high-resolution investigations is available for EDs in cubic or tetragonal perovskite structures; for example, the core structure in $SrTiO_3$ was inferred by a combination of EELS (electron

Received: November 15, 2012
Revised: February 11, 2013
Published: February 18, 2013

energy loss spectroscopy) and HRTEM,[11] and the decay of the polarization far away from an ED in a layered $SrTiO_3$/$PbZr_{0.2}Ti_{0.8}O_3$ system has been worked out by Jia et al.[12] Up to now no unit-cell-wise resolved strain and polarization map around an ED, including possibly nonlinear electromechanical coupling, has been reported. Here and in the following the phrase nonlinear refers to deviations from standard linear piezoelectric coupling with constant coupling tensors, such as occurring at strain-driven phase transitions or domain walls. The lack of information about the core structure and the surrounding limits, for example, the accuracy of phase field models[13] for explaining the dead-layer effect, the development of domain engineering techniques,[14] and the understanding of exchange bias in the presence of EDs.

In the following, we will present HRSTEM structure analysis of edge dislocations (ED) found in $BiFeO_3$ thin films. Bulk $BiFeO_3$ (Figure 1b) is pseudocubic (denoted by "pc" in the following) rhombohedral perovskite (rhombohedral angle α = 59.35° ≈ 60°, pseudocubic lattice constant a_{BFO} = 3.96 Å)[15] with a number of interesting properties (large spontaneous ferroelectric polarization P_s = 90−100 mC/cm^2, multiferroism, polymorphism).[16] Furthermore, depending on the lattice mismatch to the substrate and the associated strain, thin film configurations are reported to deviate from the bulk structure; for example, a pseudotetragonal monoclinic phase with a particularly large aspect ratio (c/a = 1.2) has been identified for large compressive strains as produced by $LaAlO_3$ substrates.[17−19] We will focus on dislocation pairs, a configuration frequently observed in our film and particularly suited for investigating strain-polarization coupling. We proceed with a short overview on the experimental details before discussing the atomic model for the ED core and analyzing unit-cell-wise strain and polarization maps of the surrounding region.

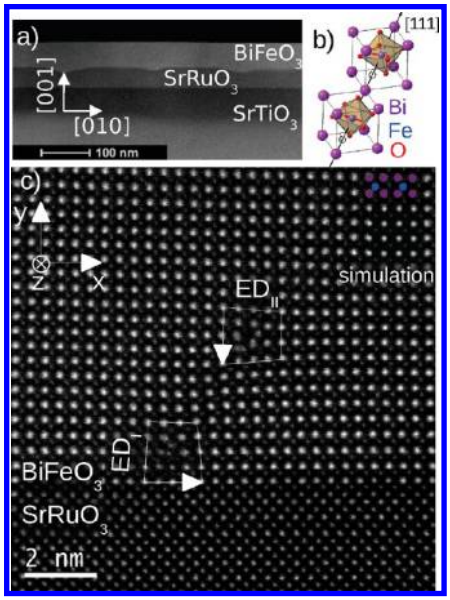

Figure 1. (a) HAADF-STEM overview of epitaxial $SrTiO_3$|$SrRuO_3$|$BiFeO_3$ thin film. The $BiFeO_3$|$SrRuO_3$ interface is not straight; i.e., it contains a large number of steps and misfit dislocations. Note that the contrast change within the $SrTiO_3$ is a thickness effect. (b) Rhombohedral $BiFeO_3$ unit cell. The polarization points into $\langle 111\rangle_{pc}$-direction appearing as $\langle 110\rangle_{pc}$ in projection. (c) High-resolution HAADF-STEM of 2 perpendicular EDs (indicated by Burgers loops) formed at the $BiFeO_3$|$SrRuO_3$ interface. In the upper right corner a HAADF STEM simulation and the projected structure of $BiFeO_3$ are depicted.

Structure Determination. An approximately 65 nm thick layer of $BiFeO_3$ was epitaxially grown in $(001)_{pc}$ orientation on a $SrRuO_3$ buffer layer (a = 0.393 nm, t = 35 nm) on top of a $SrTiO_3(001)$ single crystal substrate (a = 0.3905 nm) by pulsed laser deposition (670 °C at 100 mTorr of O_2). High-pressure reflection high-energy electron diffraction (RHEED) indicated layer-by-layer growth mode followed by step flow growth mode without any island formation. The samples were slowly cooled to room temperature in 1 atm of oxygen at a rate of 5 °C/min. The film thickness was sufficient to generate a large density of misfit EDs (see Figure 1a). The samples for TEM were prepared in cross-section geometry; they were cut parallel to the (001) planes of the $SrTiO_3$ substrate and mechanically ground to a thickness of about 20 m, followed by final liquid nitrogen-cooled ion milling under grazing incidence until electron transparency. The cooling effectively minimized possible damage of the $BiFeO_3$ thin film. A specimen thickness between 35 and 50 nm was measured by using the EELS based t/λ method.[20] High-resolution high-angle annular dark-field (HAADF) STEM[21] images of $BiFeO_3$ in [001]-direction were acquired at the aberration-corrected TEAM 0.5 microscope[22] (300 kV acceleration voltage, see Supporting Information, part I for details). We used a convergence angle of ∼19 mrad yielding a small probe size (60 pm) to resolve strong Bi columns (Z = 83) and weak FeO columns (Z = 26, 8). At a HAADF collection angle between 80 and 300 mrad the light pure O columns were not visible above the background. To determine the projected Bi and FeO atomic column positions, we used a maximum-likelihood fitting procedure[23] (see Supporting Information, part I for details): A 2D-Gaussian plus background is fitted to each atomic column starting with the strong Bi columns and taking into account previously fitted columns. Thus Bi columns are fitted before and independent from FeO neighbors, whereas the FeO column fits take into account previously determined neighboring Bi ones. Dynamic scattering simulations (see Supporting Information, part II and inset in Figure 1c) show that for the particular case of 40 nm $BiFeO_3$ imaged at 300 kV this approach is sufficient to take into account the effect of intercolumn scattering of the confined STEM probe in the fitting procedure. Depending on resolution, sample region, and column type, a fit precision ranging from 1 pm (Bi column) to 15 pm (FeO column) corresponding to eq (106) in ref 24 could be achieved. Additional systematic errors are introduced by the scanning coils and the sample drift during imaging (up to ∼50 pm characteristic shift of scanning lines in x-direction [23]) and residual zone axis misalignments or aberrations.

Dislocation Core. The first example, depicted in Figure 1c, contains a pair of two perpendicular misfit dislocations (highlighted by Burgers loops) at a distance of ∼3.4 nm, a configuration which effectively decreases the mechanical energy (see further below) of a total dislocation with $\mathbf{B} = \mathbf{B}_I + \mathbf{B}_{II} = (0,1,-1)^T a_{BFO}$ pointing in to the direction of the rhombohedral distortion (a similar ED onfiguration exists $PbTiO_3$[3]). In principle the possible core structures can be classified corresponding to the type of the glide plane (FeO_2/BiO) and the dissociation order of the dislocation. Due to fluctuations in the observed core contrasts and the missing oxygen signal, it was not possible to identify ED core structures with absolute certainty. However, the statistic of observed ED cores (3 examples are displayed in Figure 2a) in combination with data

dx.doi.org/10.1021/nl304229k | Nano Lett. 2013, 13, 1410−1415

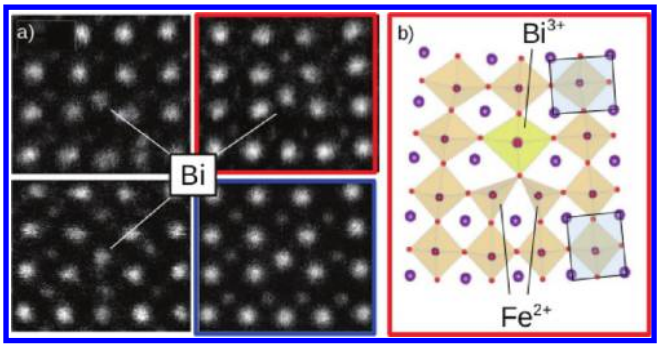

Figure 2. (a) Three examples of experimentally observed ED core contrasts and one simulated contrast (blue frame) based on the structure displayed in b. The substituted Bi is visible as bright contrast at the Fe position. (b) Proposed core structure based on computing the Bi and Fe positions from the indicated red framed experimental image and filling in the missing O. Due to the removal of one O the indicated Fe^{2+} are only 5-fold coordinated as opposed to the normal 6-fold coordination. The transparent rectangles indicate the pseudotetragonal distortion of the unit cell.

from structurally related ED cores in $SrTiO_3$[11] suggests a likely core structure (Figure 2b) with the following properties: The ED symmetrically dissociates into two half units around a centered BiO-plane. The glide plane is FeO_2. Furthermore, the original Ti position at the ED center is substituted with Bi. We now infer the oxygen positions by filling the corresponding sites in the perovskite lattice with one exception: The oxygen pair at the ED core is replaced with a single O atom because the site is too small for 2 large O^{2-} ions (Figure 2b), which is inline with oxygen deficiencies reported in case of the $SrTiO_3$ ED.[11,25] In spite of the good agreement between experimental and, based on the proposed structure, simulated HRSTEM image (Figure 2a, for details of the simulation see Supporting Information, part II) we reiterate that the oxygen positions can only be an estimate particularly neglecting structure changes along z in our case. Note that the aforementioned removal of the O atom would likely lower the valence of the two adjacent Fe atoms from Fe^{3+} to Fe^{2+}, with corresponding implications for the Fe spin state, band structure, and so forth. Additional measurements (e.g., by means of EELS) and ab initio calculations could potentially further elucidate the ED core properties including the O positions. Directly adjacent to the core highly strained perovskite unit cells are observed. In particular pseudotetragonally distorted unit cells (c/a = 1.08−1.09) form, with the long side aligned parallel or perpendicular to the Burgers vector at opposing sides of the ED (indicated by transparent rectangles in Figure 2b). To analyze the lattice structure at further distance we compile unit-cell-wise strain and polarization maps.

Strain and Polarization Maps. From the measured column positions the 2D displacement field $\mathbf{u}(\mathbf{R}_{Bi,ref}) = \mathbf{R}_{Bi} - \mathbf{R}_{Bi,ref}$ is determined, with reference positions $\mathbf{R}_{Bi,ref}$ being extrapolated by repeating a pseudocubic $BiFeO_3$ unit cell over the whole field of view. Now, engineering strain $\varepsilon(\mathbf{R})$ and rigid lattice rotation $\Omega(\mathbf{R})$ follow from the usual definitions (see Supporting Information, part III). Finally, we use the Fe displacement $\delta_{Fe}(\mathbf{R}_{Bi,ref}) = \mathbf{R}_{Fe} - \mathbf{R}_{Bi} - (0.5,0.5)^T a_{BFO}$ from the unit cell center as a measure for the 2D or projected electric polarization $\mathbf{P}(\mathbf{R}) = V_{uc}^{-1}\mathbf{Z}^*\delta_{Fe}(\mathbf{R})$, where $\mathbf{Z}^*$ is a Born effective charge tensor (BEC) and V_{uc} is the volume of the unit cell ($V_{uc}^{-1}\mathbf{Z}^* \approx -166$ mC/(cm^2 Å), see Supporting Information, part III for details). First, we note the mean polarization in the undisturbed region indicated by a dashed box in Figure 3a equals 89 ± 15 mC/cm^2 with an angular error of 5.6°, if assuming that the total polarization points along $\langle 111\rangle_{pc}$ and taking into account a certain systematic error of the BEC used here (see Supporting Information, part III). That agrees well with the reported values for the (pseudocubic) rhombohedral bulk symmetry and demonstrates the accuracy of the determined positions. The relative error of the strain within the dashed box is 3%, which corresponds well to the value obtained from error propagating the Bi position error noted previously. The corresponding strain (and polarization) maps, depicted in Figure 3, show highly strained regions in the vicinity of the EDs and almost homogeneous $BiFeO_3$ further away. The compression/tension dipoles in ε_{xx} (ε_{yy}), typical for EDs,[26] are observed at ED_I (ED_{II}) and are accompanied by a large rigid lattice rotation of some unit cells in between the two EDs (max. 5° anticlockwise). The polarization field (Figure 3a) reveals a rotation with the same sense but much larger. Indeed, a nanodomain of approximately 2 × 4 a_{BFO} in size, where in-plane polarization rotates rather abruptly about 45° into $[0\bar{1}0]_{pc}$-direction, is formed in between the EDs (see orange and red (blue) unit cells in Figure 3a (b)). By comparison with the strain map those domains could be identified as the above-

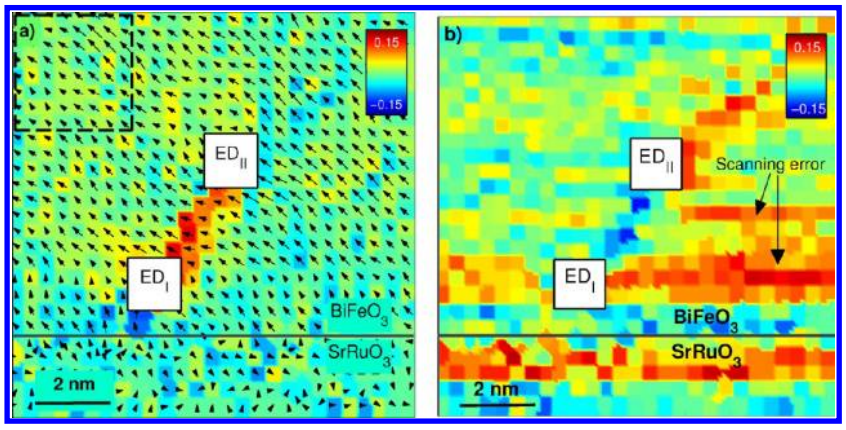

Figure 3. Experimental ε_{xx} (color), **P** (arrows with length encoding the magnitude) (a) and ε_{yy} (b) in the vicinity of 2 EDs. The dashed box in the top left corner in part a indicates the region evaluated for the bulk polarization. The experimental **P** (a) indicates the formation of a pseudotetragonal nanodomain between ED_I and ED_{II}, where polarization points into $[0\bar{1}1]_{pc}$-direction. Note the scanning error artifacts in the experimental results, i.e., straight horizontal line artifacts in ε_{yy} and **P**.

dx.doi.org/10.1021/nl304229k | Nano Lett. 2013, 13, 1410−1415

mentioned pseudotetragonal $BiFeO_3$ with a giant c/a ratio.[18] The local appearance of this pseudotetragonal phase within a strained rhombohedral surrounding is a consequence of large tensile (compressive) strains in the $x(y)$-direction driving the lattice surrounding the ED toward a critical point, where a second-order structural phase transition occurs. This is one example of nonlinear behavior that we attribute to the particular large strains around EDs. Below we will present experimental data showing characteristic coupling between EDs and DWs, which we will also explain by nonlinear coupling effects between strain and polarization in the vicinity of the EDs.

We will now gain further insight into the electromechanical coupling by comparing the previously obtained strain and polarization maps to finite element solutions of the piezoelectric-coupled system of linear elastic strain and dielectric partial differential equations, obtained from minimizing the effective total energy $G = 1/2\sigma_{ij}\varepsilon_{ij} + 1/2D_iE_i + b_{ijk}\varepsilon_{ij}E_k$ (Einstein summation convention, $\mathbf{s} \cong$ stress, $\mathbf{e} \cong$ strain, $\mathbf{D} \cong$ dielectric displacement, $\mathbf{E} \cong$ electric field, piezoelectric tensor $\mathbf{b}$, and dielectric tensor ε have been taken from literature, see Supporting Information, part IV for details of the computation including the applied boundary conditions). Already this simple model reproduces characteristic experimental findings and hence provides insight into the important mechanisms: The strain field solution of the purely elastic problem ($b_{ijk} = 0$) (Supporting Information, Figure 2) agrees very well with the piezoelectrically coupled solution and resembles qualitatively the experimental strain maps. Indeed, the conclusion that the elastic energy is the leading term in the free energy; that is, the piezoelectrically induced polarization reads $\mathbf{P}_{ind} \approx \mathbf{D} \approx \mathbf{b}\varepsilon$ (with $\mathbf{P} = \mathbf{P}_s + \mathbf{P}_{ind}$), holds for a large class of ferroelectrics, and is used within the constrained theory of ferroelectrics.[27] The deviations to the experimental strain, consisting mainly of a strong reduction of the range of the elastic strain field, stem among others from the above-mentioned formation of nanodomains not considered within the phase field simulations. Considering that the largest components of the piezoelectric tensor for rhombohedral $BiFeO_3$ are the ones linking ε_{ac} and P_a as well as ε_{cc} and P_c (see Supporting Information, part IV), it is useful to rotate the Cartesian basis 45° anticlockwise into the direction of the $BiFeO_3$ rhombohedral distortion to discuss the piezoelectric coupling: We first note that the rotated strain ε_{cc} in direction of the projected spontaneous polarization $\mathbf{P}_s$ (c-axis $\cong [0\bar{1}1]^T_{pc}$) reveals two oppositely aligned strain dipoles (Figure 4a). This coupling effectively decreases the mechanical energy which can explain the observed dislocation pair arrangement. Evaluating the induced polarization field $\mathbf{P}_{ind}$, we furthermore note that the piezoelectric coupling in the region between the 2 EDs forces the total polarization into the same direction observed experimentally in the pseudotetragonal nanodomain (Figure 3a). The calculations also predict smooth rotations of $\mathbf{P}_{ind}$ including some characteristic planes with more abrupt changes (gray lines in Figure 4b), which mainly follow the shear strain (ε_{ac}) variations. With literature values for the piezoelectric tensor (Supporting Information, part IV), however, these induced polarization variations are well below the spontaneous bulk value ($|\mathbf{P}_{ind}| \ll |\mathbf{P}_s|$ and $\mathbf{P} \approx \mathbf{P}_s$). Therefore these planes with large polarization rotation are suppressed by the spontaneous polarization $\mathbf{P}_s$ which is inline with the minor variations in $\mathbf{P}$ observed in Figure 3a. Surprisingly, however, they show up as a real DW pattern of $\mathbf{P}$ (with rather abrupt polarization rotations compared to the simulation) in the

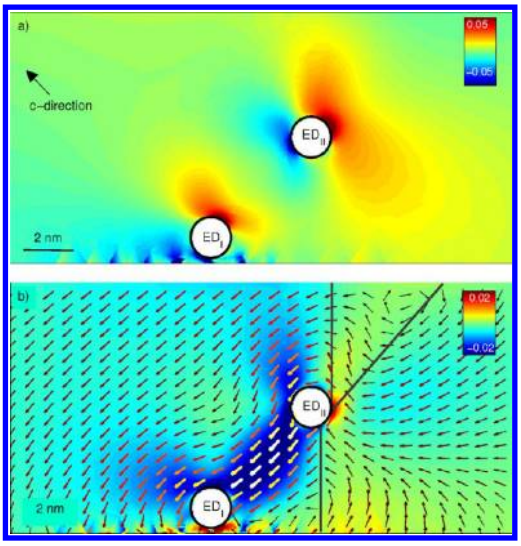

Figure 4. Simulated (a) ε_{cc} and (b) ε_{ac}, $\mathbf{P}_{ind}$ (colored arrows). Contrary to the other figures the magnitude of $\mathbf{P}_{ind}$ is here color-coded (0 = dark red, 1 mC/cm^2 = bright yellow) and clearly couples to the lattice shear ε_{ac}. Three planes of rather abrupt polarization changes are indicated by gray lines.

subsequently investigated configuration of 2 EDs (Figure 5a). Here, we identify three DWs (classified according to the DW plane and the approximate polarization rotation angle): one 109° in the $[0\bar{1}1]_{pc}$-direction (visible as 90° in-plane rotation), one 180° in the $[001]_{pc}$-direction, and an exceptional (possibly charged) tail-to-tail (tt) 109° in the $[00\bar{1}]_{pc}$-direction. They originate from ED_{II} in striking agreement with the DWs occurring in the piezoelectrically induced polarization (see Figure 4b). The agreement between calculated piezoelectrically induced and experimentally observed domain pattern suggests that the characteristic ED strain fields are the driving force behind the observed DW-ED coupling; we return to that point further below. Contrary to the first example no nanodomains could be observed in the region between the two EDs. Indeed, when performing within the red framed region indicated in Figure 4b a linear fit of the dependency of P_a from the ε_{ac}-strain component (Figure 5b inset), we obtain 364 ± 56 mC/cm^2 for that piezoelectric tensor component, which agrees well with the literature value (see Supporting Information, part IV). Here we emphasize that determining the slope of the $\mathbf{P}(\varepsilon)$ curve required a large strain interval (0−0.1) such as present only in the vicinity of the ED. At larger distance to the ED both systematic and statistical errors in particular of the polarization prevented an evaluation of the piezoelectric tensor. The large noise also prevented a potentially very interesting measurement of nonlinearities (the relative fit error of a possible quadratic component in the displayed data was around 80%) or smaller piezoelectric tensor components as well as higher-order couplings, such as flexoelectricity.[28]

We now give a possible explanation why domain walls occur in the latter system contrary to both simulations (Figure 4) and the first example (Figure 3) investigated. As already mentioned, the occurrence of the pseudotetragonal phase in the first example suggests that the strained structure around EDs in $BiFeO_3$ generally is close to a structural phase transition. There, coupling constants like the piezoelectric tensor can be drastically increased, i.e., $|\mathbf{P}_{ind}| \simeq |\mathbf{P}_s|$, especially during nonequilibrium conditions at growth. Taking into account that the nonequilibrium at growth may relax to different

dx.doi.org/10.1021/nl304229k | Nano Lett. 2013, 13, 1410−1415

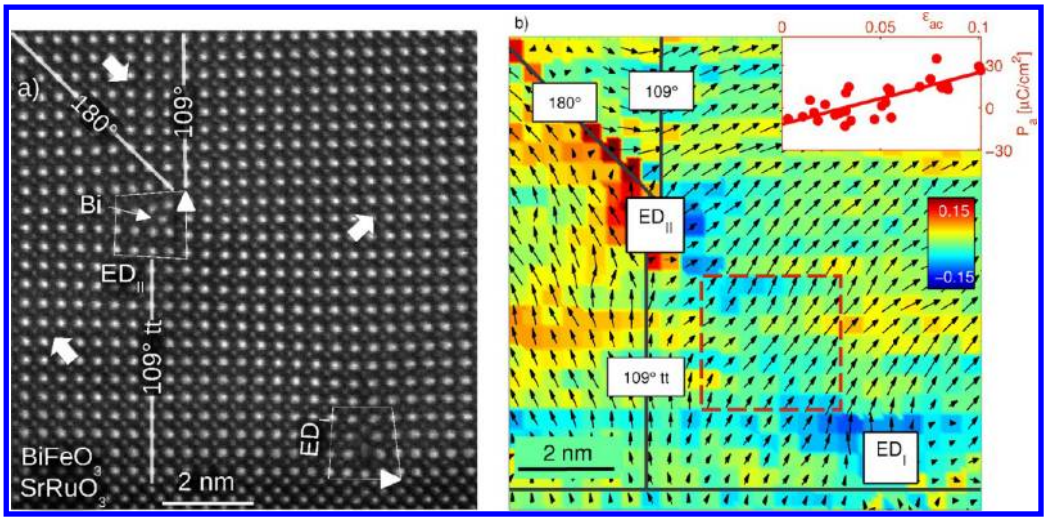

Figure 5. (a) High-resolution HAADF-STEM of twp perpendicular EDs at a distance of approximately 6.8 nm and (b) measured ε_{yy} (color) and **P** (arrows with length encoding the magnitude). The DWs are indicated by straight lines and their nominal rotation angle. The inset in the upper right corner of part b shows the polarization component P_a perpendicular to the rhombohedral distortion plotted against the strain component ε_{ac} from the dashed quadratic box. A linear fit is indicated by a solid line. An unusual tail-to-tail DW is visible below ED_{II}. Note that contrary to the first system studied (see Figures 1c, 3, and 4) ED_{II} is now left from ED_I with $\mathbf{B}_{II}$ pointing into the *y*-direction.

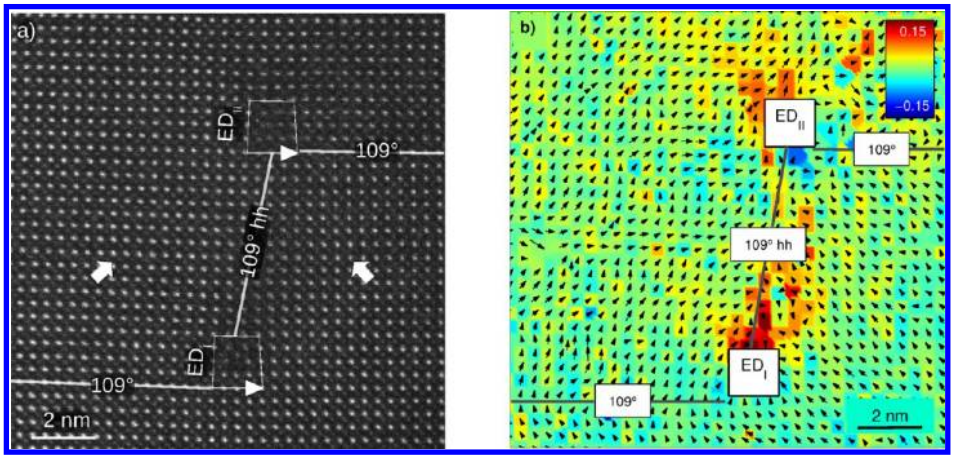

Figure 6. (a) High-resolution HAADF-STEM of two collinear EDs and (b) measured ε_{xx} (color) and **P** (arrows with length encoding the magnitude). An unusual 7 nm long head-to-head DW traced by 2 EDs intersects the 109° DW.

metastable equilibrium states, different stress and depolarization compensation routes may be statistically realized. One could be the observed formation of nanodomains, another one the formation of domain walls.

The orientation of the 109° DW parallel to the Burgers vector of the ED is also observed in another configuration shown in Figure 6. Here, a straight 109° DW contains a step traced by a system of two collinear EDs with a distance of ∼6.3 nm. This last example represents a DW pinning mechanism, which is in principle independent from the misfit introduced by the interface and can therefore attenuate the DW mobility within bulk in general. Similar to the previous example, one also observes an exceptional (possibly charged) head-to-head (hh) 109° DW in $[00\bar{1}]_{pc}$-direction. Noting that in both cases these energetically unfavorable DWs are short, we conjecture that they are locally stabilized by the strain of the EDs. We finally mention that the above shown examples represent the key characteristics from a small number of similarly coupled EDs analyzed in detail (see Supporting Information, part V), which are, however, insufficient for a statistical evaluation of the observed structures (e.g., the distance between the EDs).

Summary. We applied a dedicated model-based HAADF structure analysis to epitaxial $BiFeO_3$ thin films containing (coupled) misfit edge dislocation (ED) and domain walls (DW) to analyze details of strain-polarization coupling in the presence of strong anisotropic strain. We derived a particular $BiFeO_3$ ED core structure characterized by a replacement of Fe with Bi and the removal of one O column. Both effects have a large impact on the local spin arrangement and hence the exchange bias stimulated by ED defects. Within the highly strained region close to the ED a variety of structures attributed to nonlinear strain-polarization coupling was observed. The local formation of pseudotetragonal $BiFeO_3$ nanodomains within the strained rhombohedral matrix suggests critical behavior close to EDs in $BiFeO_3$. We quantitatively determined the largest piezoelectric tensor component directly from the HAADF data and identified a piezoelectrically driven pinning or growth mechanism of 109° (and 180°) DWs parallel (and 45° inclined) to the Burgers vector of the ED. Furthermore, locally confined and possibly charged head-to-head and tail-to-tail DWs coupled to EDs have been observed. To which extend the observed nanodomains, morphotropic phase boundaries

dx.doi.org/10.1021/nl304229k | *Nano Lett.* 2013, 13, 1410−1415

and DWs around EDs transfer to other materials depend on the particular strain-dependent phase diagrams, crystal symmetries, and the resulting piezoelectric coupling and have to be analyzed by further studies. From a broader perspective we showed that misfit EDs in $BiFeO_3$ exert a short-range (ED-ED and ED-nanodomain coupling) and long-range (ED-DW coupling) influence on the ferroelectric thin film which both lead to a reduction of overall ferroelectric properties of the thin film.

■ ASSOCIATED CONTENT

Supporting Information

HAADF STEM structure analysis (part I); HAADF image simulations (part II); displacement field, strain tensor, and electric polarization (part III); phase field edge dislocation models (part IV); supplementary HAADF images and strain maps. This material is available free of charge via the Internet at http://pubs.acs.org.

■ AUTHOR INFORMATION

Corresponding Author

*E-mail: Axel.Lubk@triebenberg.de.

Notes

The authors declare no competing financial interest.

■ ACKNOWLEDGMENTS

The authors acknowledge financial support from the European Union under the Seventh Framework Programme under a contract for an Integrated Infrastructure Initiative Reference 312483-ESTEEM2.

■ REFERENCES

(1) Chu, M.-W.; Szafraniak, I.; Scholz, R.; Harnagea, C.; Hesse, D.; Alexe, M.; Gosele, U. *Nat. Mater.* **2004**, *3*, 87−90.
(2) Sun, H. P.; Tian, W.; Pan, X. Q.; Haeni, J. H.; Schlom, D. G. *Appl. Phys. Lett.* **2004**, *84*, 3298−3300.
(3) Nagarajan, V.; Prasertchoung, S.; Zhao, T.; Zheng, H.; Ouyang, J.; Ramesh, R.; Tian, W.; Pan, X. Q.; Kim, D. M.; Eom, C. B.; Kohlstedt, H.; Waser, R. *Appl. Phys. Lett.* **2004**, *84*, 5225−5227.
(4) Misirlioglu, I. B.; Vasiliev, A. L.; Aindow, M.; Alpay, S. P. *Integr. Ferroelectr.* **2005**, *71*, 67−80.
(5) Canedy, C. L.; Li, H.; Alpay, S. P.; Salamanca-Riba, L.; Roytburd, A. L.; Ramesh, R. *Appl. Phys. Lett.* **2000**, *77*, 1695−1697.
(6) Emelyanov, A. Y.; Pertsev, N. A. *Phys. Rev. B* **2003**, *68*, 214103.
(7) Chu, M.-W.; Szafraniak, I.; Hesse, D.; Alexe, M.; Gösele, U. *Phys. Rev. B* **2005**, *72*, 174112.
(8) Su, D.; Meng, Q.; Vaz, C. A. F.; Han, M.-G.; Segal, Y.; Walker, F. J.; Sawicki, M.; Broadbridge, C.; Ahn, C. H. *Appl. Phys. Lett.* **2011**, *99*, 102902.
(9) Martin, L. W.; Chu, Y.-H.; Holcomb, M. B.; Huijben, M.; Yu, P.; Han, S.-J.; Lee, D.; Wang, S. X.; Ramesh, R. *Nano Lett.* **2008**, *8*, 2050−2055.
(10) Lymperakis, L.; Neugebauer, J.; Albrecht, M.; Remmele, T.; Strunk, H. P. *Phys. Rev. Lett.* **2004**, *93*, 196401.
(11) Zhang, Z.; Sigle, W.; Rühle, M. *Phys. Rev. B* **2002**, *66*, 094108.
(12) Jia, C. L.; Mi, S. B.; Urban, K.; Vrejoiu, I.; Alexe, M.; Hesse, D. *Phys. Rev. Lett.* **2009**, *102*, 117601.
(13) Alpay, S. P.; Misirlioglu, I. B.; Nagarajan, V.; Ramesh, R. *Appl. Phys. Lett.* **2004**, *85*, 2044−2046.
(14) Jang, H. W.; Ortiz, D.; Baek, S.-H.; Folkman, C. M.; Das, R. R.; Shafer, P.; Chen, Y.; Nelson, C. T.; Pan, X.; Ramesh, R.; Eom, C.-B. *Adv. Mater.* **2009**, *21*, 817−823.
(15) Kubel, F.; Schmid, H. *Acta Crystallogr., B* **1990**, *46*, 698−702.
(16) Catalan, G.; Scott, J. F. *Adv. Mater.* **2009**, *21*, 2463−2485.
(17) Ricinschi, D.; Yun, K.-Y.; Okuyama, M. *J. Phys.: Condens. Matter* **2006**, *18*, L97.
(18) Béa, H.; Dupé, B.; Fusil, S.; Mattana, R.; Jacquet, E.; Warot-Fonrose, B.; Wilhelm, F.; Rogalev, A.; Petit, S.; Cros, V.; et al. *Phys. Rev. Lett.* **2009**, *102*, 217603.
(19) Rossell, M. D.; Erni, R.; Prange, M. P.; Idrobo, J.-C.; Luo, W.; Zeches, R. J.; Pantelides, S. T.; Ramesh, R. *Phys. Rev. Lett.* **2012**, *108*, 047601.
(20) Malis, T.; Cheng, C., S.; Egerton, R. F. *J. Electr. Microsc. Techn.* **1988**, *8*, 193−200.
(21) Erni, R.; Rossell, M. D.; Kisielowski, C.; Dahmen, U. *Phys. Rev. Lett.* **2009**, *102*, 096101.
(22) Kisielowski, C.; Freitag, B.; Bischoff, M.; Van Lin, H.; Lazar, S.; Knippels, G.; Tiemeijer, P.; Van Der Stam, M.; Von Harrach, S.; Stekelenburg, M.; et al. *Microsc. Microanal.* **2008**, *14*, 469−477.
(23) Lubk, A.; Rossell, M. D.; Seidel, J.; He, Q.; Yang, S. Y.; Chu, Y. H.; Ramesh, R.; Hÿtch, M. J.; Snoeck, E. *Phys. Rev. Lett.* **2012**, *109*, 047601.
(24) den Dekker, A. J.; Van Aert, S.; van den Bos, A.; Van Dyck, D. *Ultramicroscopy* **2005**, *104*, 83−106.
(25) Jia, C. L.; Thust, A.; Urban, K. *Phys. Rev. Lett.* **2005**, *95*, 225506.
(26) Hirth, J.; Lothe, J. *Theory of Dislocations*; McGraw-Hill series in materials science and engineering; McGraw-Hill: New York, 1967.
(27) Li, L.; Yang, Y.; Shu, Y.; Li, J. *J. Mech. Phys. Solids* **2010**, *58*, 1613−1627.
(28) Catalan, G.; Lubk, A.; Vlooswijk, A. H. G.; Snoeck, E.; Magen, C.; Janssens, A.; Rispens, G.; Rijnders, G.; Blank, D. H. A.; Noheda, B. *Nat. Mater.* **2011**, *10*, 963−967.